Co-metal induced stabilization of alumina-supported copper: impact on the hydrogenolysis of glycerol to 1,2-propanediol

Alexandra Bouriakova, Pedro S. F. Mendes, Benjamin Katryniok, Jeriffa de Clercq, Joris W. Thybaut

Insight into the mechanism of glycerol hydrogenolysis to 1,2-propanediol: benefits of Cu promotion by La

Alexandra Bouriakova[a], Pedro S. F. Mendes[a], Robert Wojcieszak[b], Christophe Detavernier[c]

Benjamin Katryniok[b], Jeriffa De Clercq[d], Joris W. Thybaut[a]*

[a] Laboratory for Chemical Technology, Department of Materials, Textiles and Chemical Engineering, Ghent University, Technologiepark 125, 9052 Zwijnaarde, Belgium

[b] Univ. Lille, CNRS, Centrale Lille, Univ. Artois, UMR 8181 - UCCS - Unité de Catalyse et Chimie du Solide, F-59000 Lille, France

[c] Conformal Coating of Nanomaterial, Department of Solid State Sciences, Ghent University, Krijgslaan 281/S1, 9000 Ghent, Belgium

[d] Industrial Catalysis and Adsorption Technology, Department of Materials, Textiles and Chemical Engineering, Ghent University, Valentin Vaerwyckweg 1, 9000 Ghent, Belgium

[*]corresponding author: Joris.Thybaut@UGent.be

Abstract

The effect of La promotion on a Cu/γ-Al$_2$O$_3$ catalyst for glycerol hydrogenolysis towards 1,2-propanediol, as alternative for its petroleum based production route, was investigated under continuous flow operation in a trickle bed reactor. The La-Cu interaction led to co-existence of Cu$^+$ and Cu^0 species. The activity rather decreased with La/Cu ratio, owing to a tradeoff between stability and activity. Sintering of the Cu particles occurred, but was less pronounced in the presence of La. Characterization showed that with increasing La/Cu ratio, the number of weak and moderate acid sites increased while that of the strong acid sites decreased. Our results indicate that Cu$^+$, rather than the support, plays a key role in the acetol formation and consequently in the selectivity towards 1,2-propanediol. Compared to a Cu catalyst, the La-Cu one exhibited a better glycerol conversion stability over time (relative decrease of 12.5% vs. 25%) and 1,2-propanediol selectivity (94% vs. 82%).

1 Introduction

Glycerol has emerged as a biomass-based feedstock in the chemical, solvent and fuel industry.[1-3] The majority (60-70 %) of the natural glycerol is co-produced with biodiesel by transesterification, the resulting mixture containing approximately 10 vol.% of glycerol.[3, 4] It is one of the key platform chemicals in these industries thanks to its unique chemical versatility originating from the three hydroxyl groups on its C3-backbone. In a hydrogenolysis reaction, the cleavage of a C-O or C-C bond occurs simultaneously with hydrogen addition.[5] The cleavage of a primary C-O bond in glycerol results in 1,2-propanediol (*i.e.* propylene glycol), while that of the secondary C-O yields 1,3-propanediol. 1,2-propanediol has a wide range of applications depending on its purity, including

36 food, pharmaceuticals, cosmetics, as a monomer for resins, aircraft deicing fluids, automotive

37 coolants, paints and coatings, liquid detergents, inks, varnishes, tobacco humectants, etc.[6]

38 Currently, it is produced from the petroleum derived and explosive propylene oxide, in the presence

39 of an acid catalyst.[6] Thus, the valorization of glycerol contributes to the development of safer and

40 sustainable production route for currently petroleum-based 1,2-propanediol.

41 Cu-based catalysts are often applied in industry due to their lower price compared to noble metals

42 and their enhanced selectivity to C-O bond cleavage, which is higher compared to Co- or Ni-

43 catalysts.[7, 8] Initially, many industrially used commercial Cu catalysts have been investigated for

44 glycerol hydrogenolysis.[9-14] Later, other Cu-based supported over MgO[15-17], SiO_2[18-22] or

45 Al_2O_3[23-33] were also reported by various researchers.

46 Significant efforts have been made in preparing effective and stable Cu-based catalysts in the last

47 two decades. Typically, promoters are required to limit the tendency of Cu to sinter.[34-37]

48 Undoubtedly, the Cu dispersion and/or interaction between Cu species, the support, and a

49 promotor are the main factors in determining the catalytic activity, selectivity and stability. In our

50 previous work[38], Ba, Ce, Cs and La were investigated as dopants, *c.q.* promoters, for the

51 hydrogenolysis of glycerol into 1,2-propanediol over a Cu/γ-Al_2O_3 catalyst. The addition of Ba or Ce

52 increased the initial activity, while La allowed to establish the most stable activity in terms of glycerol

53 conversion over time (relative decrease of ca. 25 % over 68 h time on stream).

54 Two alternative mechanisms are mainly reported in the literature for the production of

55 1,2-propanediol from glycerol: the dehydration-hydrogenation mechanism (involving acidic sites)

56 [39, 40] and the dehydrogenation-dehydration-hydrogenation mechanism (involving basic

57 sites)[41]. It is commonly accepted that γ-Al_2O_3 has intrinsic acidity[42], automatically leading to the

58 assumption that the hydrogenolysis of glycerol proceeds according to the dehydration-

59 hydrogenation mechanism on Cu based catalysts. In this case, the dehydration step would occur on

60 an acid site, available on the support, while the hydrogenation step is then catalyzed by a Cu^0

61 particle. However, various researchers are convinced that Cu^0 is the active site for both steps in the

62 dehydration-hydrogenation mechanism.[43-46] Other researchers believe in the synergetic effect

63 between Cu^+ and Cu^0, or in the role of Cu^+ as active site, i.e., assuming that Cu is not entirely present

64 in the pure metallic state.[11, 19, 21, 33, 47-49] Vila *et al.*[27] pointed out that Cu^+ species in a Cu/γ-

65 Al_2O_3 catalyst improved the glycerol conversion, while the differences in 1,2-propanediol selectivity

66 could be related to the different Cu^0/Cu^+ in the catalysts. Generally, Cu catalysts show a high

67 selectivity towards 1,2-propanediol, however, some C-C cleavage to 1,2-ethanediol can be

68 observed. The retro-aldol condensation reaction that leads to the C-C cleavage, requires hydrogen.

69 Hence, it is commonly accepted that it is catalyzed by a metallic site, in this case Cu^0.[50-52]

70 However, the effect of strong acidic sites cannot be ruled out in a C-C cleavage.[51, 53] To elucidate

71 the role of the different Cu species, a well-controlled preparation of catalysts with various Cu^+ or

72 Cu^0 amounts is necessary. La was found to impact on the presence of Cu^+ and Cu^0 sites in Cu/SiO_2

73 catalysts.[54, 55] Insights in this respect on γ-Al_2O_3 supported Cu catalysts for glycerol

74 hydrogenolysis are, however, still lacking.

75   In this work, we aim to investigate the effect of La promotion on γ-Al_2O_3 supported Cu species to

76 gain insight into their catalytic mechanism for glycerol hydrogenolysis. To this end, a series of

77 La-Cu catalysts was prepared by sequential impregnation. By varying the La and Cu loading, twelve

78 different promotion ratios were obtained with various distribution of the Cu^+ and Cu^0 species. The

79 catalysts were comprehensively characterized in terms of textural and physicochemical properties,

80 crystallographic and morphological structure, reduction behavior and surface species to better

81 understand the effect of the promotion ratio. We selected five La-Cu catalysts, with specific

82 characteristics, to perform liquid phase glycerol hydrogenolysis in a fixed bed reactor operated in

83 trickle flow regime and compared them to a bare Cu catalyst. The effect of the La/Cu mass ratio was

84 investigated by comparing the surface species, catalysts activity and 1,2-propanediol selectivity for

85 these six catalysts. The catalysts stability was investigated by comparing the Cu^0 particle size *prior*

86 and *post* reaction.

87 **2   Experimental**

88 **2.1   Catalyst synthesis**

89   All the catalysts in this work, indicated as *x*La-*y*Cu/γ-Al$_2$O$_3$, in which *x* and *y* are the corresponding

90 weight percentage (wt.%), were synthesized using a sequential wet impregnation method. The La

91 and Cu loading varied between 0 and 2.5 wt.%, and 10 and 25 wt.%, respectively. In this method,

92 the support, γ-Al$_2$O$_3$ (Sasol, Puralox SCCa-150/200), was suspended in 10 ml demineralized water

93 per gram of support. At the same time, the promoter precursor, La(NO$_3$)$_3$.6H$_2$O (Sigma-Aldrich, ≥ 99

94 %), was dissolved in 6.6 ml distilled water per wt.% of La. The suspensions were mixed and stirred

95 at 500 rpm at room temperature for 2 h. Subsequently, the water was evaporated at 363 K, after

96 which the sample was further dried in air at 393 K for 1.5 h and calcined at 673 K, using a ramp of 2

97 K min^{-1} in static air for 2 h. In the second step, the *x* wt.% La/γ-Al$_2$O$_3$ powder was suspended in 150

98 mL demineralized water, mixed and stirred at 500 rpm for 2 h with the desired amount of metal

99 precursor, Cu(NO$_3$)$_2$.5/2H$_2$O (Sigma-Aldrich, ≥ 99 %), which was dissolved in 75 mL demineralized

100 water. The catalyst was obtained after the same thermal treatment as in the La-loading step. For

101 comparison, a bare Cu/γ-Al$_2$O$_3$ catalyst was also prepared.

2.2   Catalyst characterization

103   The elemental analysis was performed by inductively coupled plasma-optic emission

104   spectroscopy over a 720-ES ICP-OES equipment (Agilent) with axial viewing and simultaneous

105   Charge Coupled Device detection. Before the elemental analysis, the sample was prepared by

106   dissolving 10 mg of dried and grounded sample in concentrated aqua regia solution (HNO_3:HCl, 1:3,

107   v:v). The solution was heated to 383 K during 2 h in the autodigestor Vulcan 42 (Questron) and

108   diluted up to 20 ml with ultrapure water before analysis.

109   The specific surface area and pore volume of the catalyst were measured through N_2-sorption

110   experiments at 77 K using a Tristar II 3020 Micrometrics apparatus. The specific surface area, S_{BET},

111   was determined using the five-point Brunauer-Emmett-Teller method. The total pore volume, V_p,

112   was estimated from the adsorbed nitrogen amount at relative pressure of 0.98. The pore size

113   distribution and average pore size, D_p, were calculated according the Barrett-Joyner-Halenda

114   formula applied to the desorption isotherm.

115   Powder X-ray diffraction (XRD) patterns were obtained using a Bruker D8-AXS Discover device

116   and a linear Vantec detector, using with a CuK_α X-ray source (λ = 1.54 Å) under continuous scan

117   mode over a 2θ range of 15° to 75°, with a step size of 0.02°.[56] The reduction was performed *in-*

118   *situ* with 5 vol.% H_2-He at 1.1 NmL s^{-1} with a temperature increase up to 723 K (ramp: 8 K min^{-1}). For

119   the presentation of the results, the observed intensity was normalized based on the intensity of the

120   highest peak. The Scherrer equation, was used to determine the size of the crystals in the calcined,

121   reduced or spent catalysts.

122   The dispersion, D_{Cu^0}, the mean Cu surface area, MSA_{Cu^0}, and the average diameter of the Cu

123   aggregates, $\emptyset_{Cu^0}$, were determined by dissociative N_2O adsorption according to the method of

124 Gervasini *et al.*[57] on the Micrometrics Autochem II 2920 equipped with a TCD-detector. This

125 method determines the D_{Cu^o}, and MSA_{Cu^o} with qualitative and quantitative information by a

126 successive analysis of H_2-TPR, a surface oxidation by N_2O and the H_2-TPR of the freshly oxidized Cu

127 surface (defined as s-TPR). s-TPR allows to distinguish between surface Cu species and bulk Cu.[57]

128 To desorb any potentially adsorbed species, the temperature was first increased to 473 K (ramp: 90

129 K min^{-1}), held constant for 5 min, and cooled to 323 K. In the next step, the reducibility of the

130 catalysts was evaluated by H_2-TPR, pursuing complete reduction of CuO to Cu^0. A gaseous 10%H_2-Ar

131 mixture with a flow rate of 1 NmL s^{-1} was sent over the catalyst while heating to 723 K at a ramp of

132 8 K min^{-1}. Once at 723 K, the temperature was held constant for 30 min during which the Cu^x species

133 were reduced to Cu^0. Next, the temperature was reduced to 323 K. In the second step, a constant

134 flow of 1 vol.% N_2O-Ar gas with a flow rate of 0.25 NmL s^{-1} (Air Liquide) was sent over the catalyst at

135 323 K for 1 h, during which surface Cu^0 species reacted with N_2O and formed Cu^+. In the third step

136 again a 10 vol.% H_2-Ar gas at a flow rate of 1 NmL s^{-1} was sent over the catalyst, while heating this

137 time to 1073 K (ramp: 20 K min^{-1}) thereby reducing the surface Cu^+ species to Cu^0. The amount of

138 consumed H_2 was measured by a thermal conductivity detector (TCD). The Cu dispersion, D_{Cu^o},

139 defined as the ratio of the Cu exposed at the surface to the total amount Cu, was calculated from

140 the amount of H_2 consumed in the s-TPR analysis. The mean Cu surface area, MSA_{Cu^o} [m² g$^{-1}_{cat}$], is

141 a measure for the number of active sites on the catalyst and calculated with equation (1), in which

142 n_{H_2} stands for the experimentally consumed number of moles of H_2 [μmol$_{H2}$ g$^{-1}_{cat}$], SF is the

143 assumed O/Cu ratio (2 mol$_{Cu}$ mol$^{-1}_{H2}$), N_A is the Avogadro's number and C_M is the average number

144 of Cu atoms per area, assuming equally exposed (100), (110) and (111) planes, i.e.

145 1.47 10^{19} atoms$_{Cu}$ m$^{-2}_{Cu}$.

$$MSA_{Cu^o} = \frac{n_{H_2} \cdot SF \cdot N_A}{10^6 \cdot C_M} \tag{1}$$

146   The average diameter of the Cu aggregates, $\emptyset_{Cu^o}$ [nm], is determined from MSA_{Cu^o} via Eq. (2),

147   where SK is a constant representing the available surface area of a particle (SK = 5) and ρ_{Cu} the

148   density of Cu (8.92 g cm^{-3}).

$$\emptyset_{Cu^o} = \frac{10^3 \cdot SK \cdot wt.\%_{Cu}}{MSA_{Cu^o} \cdot \rho_{Cu}} \tag{2}$$

149   For the determination of acid sites, ammonia (NH$_3$) was used as a probe molecule during TPD. For

150   the measurement of the total number of acid sites, *ca.* 0.2 g of catalyst (or pure support) was diluted

151   with 0.8 g of inert material. First, this diluted sample was heated in an inert atmosphere (Ar, 0.42

152   NmL s^{-1}) up to 473 K (ramp: 90 K min^{-1}). After 5 min, the temperature was decreased to 383 K and

153   kept at that temperature for 20 min. Next, the catalyst was reduced using 10 vol.%H$_2$-Ar (1 NmL s^{-1})

154   while heating to 473 K (ramp: 8 K min^{-1}) after which the temperature was kept for 15 min. After the

155   reduction, the temperature was decreased to 423 K and the gas flow was switched to 4 vol.% NH$_3$-

156   He with a flow rate of 0.25 NmL s^{-1}. After 30 min, the gas was switched to Ar (0.42 NmL s^{-1}) to remove

157   the physisorbed NH$_3$. Finally, the temperature was increased to 873 K at a heating rate of 10 K

158   min^{-1}. The amount of desorbed NH$_3$ was detected by a TCD.

159   The composition and oxidation state of the elements present on the catalysts surface were

160   determined using X-ray photoelectron spectroscopy (XPS). The XPS spectra were recorded at a

161   residual pressure of 10^{-9} mbar on a Kratos Axis UltraDLD electron energy spectrometer operating

162   with a monochromatic Al-Kα (1486.6 eV). The pass energy of the hemispherical analyzer was set at

163   160 eV for the wide scan and 40 eV for narrow scans. In the latter conditions, the full width at half

164   maximum (FWHW) of the Ag 3d$_{5/2}$ peak of a standard silver sample was about 0.9 eV. Charge

165 stabilization was achieved by using the Kratos Axis device. Peak decomposition was performed using

166 curves with a 70% Gaussian type and a 30% Lorentzian type and a Shirley nonlinear sigmoid-type

167 baseline. The following peaks were used for the quantitative analysis: O 1s, C 1s, La 3d, Cu 2p, and

168 Cu LMM Auger peak. Molar fractions were calculated using peak areas normalized on the basis of

169 acquisition parameters after a Shirley background subtraction and corrected with experimental

170 sensitivity factors and transmission factors provided by the manufacturer. The binding energy (BE)

171 scale was calibrated by measuring C 1s peak (BE = 284.8 eV) from the surface contamination and

172 the accuracy of the measurement was ± 0.1 eV. Differential surface charging of the samples was

173 ruled out by checking the reproducibility of XPS measurements in repeated scans under different X-

174 ray exposures. Software CasaXPS was used for the analysis of XPS spectra, separating elemental

175 species in different oxidation states, and calculating relative concentrations of chemical elements.

176 Scanning (Transmission) Electron Microscopy was performed with a Cs corrected JEOL JEM-2200FS

177 instrument[58] equipped with a Schottky-type field-emission gun and JEOL JED-2300D energy-

178 dispersive X-ray (EDX) detector, at 200 kV. Specimen preparation consisted of immersing a lacey

179 carbon film supported on a Ni grid into the sample powder. Dark-field STEM images give the best

180 contrast to the identification of particles. For the spent 1.5La-10Cu, 1.5La-20Cu, 2.0La-10Cu and

181 2.0La-20Cu catalysts, the particle size distribution of the large particle population (> 10 nm) was

182 determined based on almost 500 particles. For the 1.0La-10Cu catalyst, the particle size distribution

183 was established on 117 particles, due to a limited amount of STEM images. For the 10Cu catalyst,

184 only 30 particles were measured as sintering was clear on every image.

185 **2.3 Catalyst performance testing**

186 The performance of the catalysts was assessed for liquid phase glycerol (99.5%, Sigma-Aldrich)

187 hydrogenolysis in a high-throughput kinetics mechanistic investigation set-up.[59] The reaction was

188 performed within the intrinsic kinetic regime, which was assessed by typical correlations[60, 61] and

189 experimentally proven in previous work[46], under steady state conditions in a fixed bed reactor

190 operating in a trickle-bed regime.

191 The reactor effluent was analyzed using a gas chromatograph equipped with a flame ionization

192 detector and an Agilent CP-Was 57 CB glycols column using 1,4-butanediol as an external standard.

193 The calibration factors are listed in Table SI.1.

194 Conversion was defined according to equation (3), where F_G^0 and F_G represent respectively the

195 molar in- and outlet flow rates of glycerol (mol s^{-1}).

$$X_G = \frac{F_G^0 - F_G}{F_G^0} \tag{3}$$

196 The selectivity towards a component i was calculated on a molar carbon basis according to

197 equation (4), with $a_{c,G}$ the number of carbon atoms in glycerol, F_i^0 and F_i the molar in- and outlet

198 flow rates of a component i (mol s^{-1}) respectively.

$$S_{i,G} = \frac{a_{c,i} \cdot \left(F_i - F_i^0\right)}{a_{c,G} \cdot \left(F_G - F_G^0\right)} \tag{4}$$

199 The activity is defined as the ratio of the mass flow rate in which glycerol is converted,

200 $\dot{m}_{G,converted}$ (kg$_G$ s^{-1}), to the total amount of catalyst used, W_{cat} (kg$_{cat}$).

$$activity = \frac{\dot{m}_{G,converted}}{W_{cat}} \tag{5}$$

3 Results and discussion

Industrially, a high density of active sites on the catalysts, which is mostly achieved at high metal loadings, is desirable to maximize the volumetric activity. However, to prove relationships between catalyst structure and catalytic performance, more moderate metal loadings (< 20 wt.%) are advisable [62, 63]. In our previous work[38], it was clear that a small amount of 1.0 wt.% of La sufficed to increase the stability of a 10 wt.% of Cu/Al_2O_3 catalyst. In this work, the La/Cu mass ratio was varied around that central point, aiming at changing the distribution of the Cu^+ and Cu^0 species. Therefore, a series of La-Cu/γ-Al_2O_3 catalysts with nominal La and Cu values: x wt.% La – 10 wt.% Cu (x = 0, 1.0, 1.5, 2.0), x wt.% La – y wt.% Cu (x = 1.5, 2.0, 2.5 and y = 15, 20, 25) were prepared.

No lanthanum was leached during the synthesis as the La loading in the intermediate La/γ-Al_2O_3 materials was similar as for the La-Cu/γ-Al_2O_3 catalyst (Table SI.2). The actual La and Cu loadings in the calcined catalysts were systematically lower than the nominal ones, Table SI.3. This was attributed to the hygroscopic nature of the precursors, leading to an overestimation of the actually introduced amounts during the synthesis.

To understand the nature of the Cu species present on the catalyst's surface and their evolution, the catalysts were characterized in three states: after calcination, after reduction and *post*-reaction (*i.e.* spent catalyst). On that ground, the role of Cu species in the catalytic performance for glycerol hydrogenolysis was investigated.

3.1 Catalyst characterization

3.1.1 Textural properties

The support and the catalysts were characterized by N_2 sorption. A type-IV N_2-adsorption isotherm is observed for all catalysts, see Figure 1 and Figure SI.1, which is expected since the support (PURALOX® γ-Al_2O_3) is mesoporous.[64] The presence of mesopores (2 – 50 nm) is confirmed by the pore size distribution (Table SI.3). The hysteresis loops are classified as type H1, which is typical for materials with cylindrical pore channels.[65] The BET surface area exhibits a small decrease upon the La and Cu impregnation without a clear trend as a function of metal loading or promotor ratio. A similar observation was made for the mesoporous volume and the mean pore volume or size. The BET surface area ranged between 164 and 192 $m^2\,g^{-1}_{support}$ (Table SI.3) while the mesoporous volume and mean pore size varied between 0.38 – 0.47 $cm^3\,g^{-1}_{support}$ and 6.4 – 8.6 nm, respectively (Table SI.3). Therefore, it is concluded that the promotion has no significant impact on the textural properties of the support.
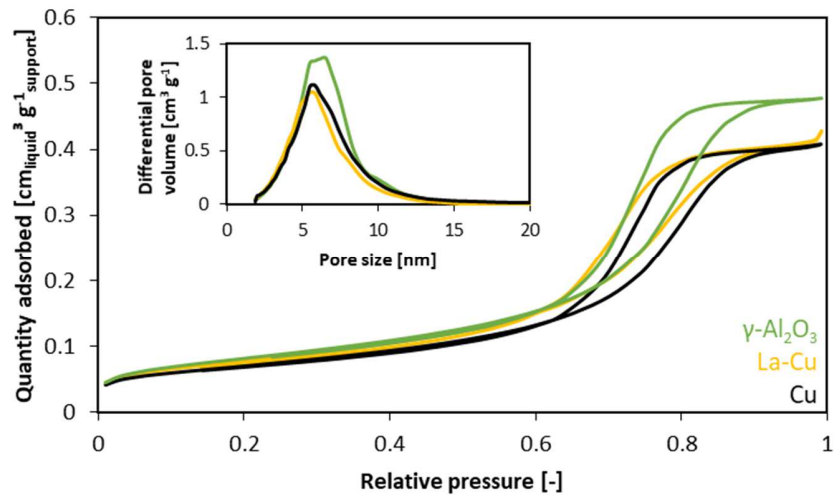
Figure 1. N_2-sorption isotherms and differential pore size distribution of the support (green), 10Cu catalyst (black) and 1.0La-10Cu (yellow) catalysts, as representative for the La-Cu catalysts.

12

3.1.2 Crystallographic and morphological structure

The crystalline phases of the support and the calcined and reduced catalysts were determined by XRD, as shown in Figure 2 and Figure SI.2. Broad diffraction peaks for γ-Al_2O_3 at 31.8°, 37.5°, 39.2°, and 45.7°, respectively corresponding to the $Al_2O_{3(220)}$, $Al_2O_{3(311)}$, $Al_2O_{3(222)}$, $Al_2O_{3(400)}$ facets are detected for all catalysts, see Figure 2. This indicates a limited crystallinity of the support. The calcined La-Cu catalysts exhibited main characteristic diffraction peaks of $CuO_{(002)}$ at 35.4° and $CuO_{(111)}$ at 38.6°, and minor diffraction peaks at 32.5° ($CuO_{(-110)}$), 48.7° ($CuO_{(-202)}$), 51.4° ($CuO_{(112)}$) and 53.5° ($CuO_{(020)}$). For none of the catalysts, the most characteristic peak of $Cu_2O_{(111)}$ at 36.4° could be detected. Therefore, it can be deduced that, if present, Cu_2O was either highly dispersed or amorphous, or in a very little amount. As the La-loading was below 8.5 μmol_{La} m^{-2}[66], the characteristic peaks of lanthanum oxides (La_2O_3 and LaO) were not observed. The main diffraction peaks of the mixed Cu-Al phase, $CuAl_2O_{4(400)}$ at 36.8° and $CuAlO_{2(012)}$ at 37.1°, overlap with the broad diffraction peak for $Al_2O_{3(311)}$. Most likely, those phases were not present, as they only form above 773 K, according to the CuO-Al_2O_3 phase diagram.[67, 68]

After reduction at 723 K, the representative Cu^0 XRD peaks appeared at 43.3° for $Cu^0_{(111)}$ and at 50.5° for $Cu^0_{(200)}$. No characteristic peaks of CuO remained and, again, no characteristic peak of Cu_2O at 36.4° was identified, impeding any conclusion on Cu_2O. Based on the Scherrer equation, the Cu^0 crystallite sizes were in the range from 40 nm to 80 nm (Table SI.4), while on the calcined, *i.e.* prior to the reduction, catalysts the CuO crystallite sizes were calculated in the range of 20 to 40 nm (Table SI.2).e. This indicates that during the reduction, the Cu crystallites doubled in size compared to the initial CuO.

256

262 To study the evolution of the Cu oxidation state during the reduction, the 1.0La-10Cu catalyst was

263 investigated by means of *in situ* XRD, see Figure 3. The characteristic peaks of CuO at 32.5°, 35.4°,

264 38.6° and 48.7° decrease between 500 and 520 K in favor of the Cu^0 main peaks at 43.3° and 50.5°.

265 The broad diffraction peaks for γ-Al$_2$O$_3$ at 39.2 and 45.7° kept their intensity during the reduction

266 process. However, it is clear that the intensity between 34.5° and 38.6° changes during the reduction

267 process. This area does not only correspond to the pattern of γ-Al$_2$O$_{3,(311)}$ but also to Cu$_2$O$_{(111)}$ and

268 the mixed Cu-Al phases, CuAlO$_2$ and CuAl$_2$O$_4$, most likely indicating (some) reduction of the Cu

269 species. On the other hand, an increase in intensity at around 42.3°, corresponding to Cu$_2$O$_{(200)}$,

270 could also be observed in Figure 3. The low intensity of the Cu$_2$O species is most likely due to the

271 low amount (and crystallinity) of Cu$_2$O and, hence, its presence was further investigated by XPS, see

272 section 3.1.4. Whereas Cu$_2$O could not be observed in the regular XRD measurements of the calcined

273 and reduced catalysts, thanks to the *in situ* XRD it appears that in the calcined catalyst Cu$_2$O mainly

274 consists of $Cu_2O_{[111]}$, with a minor amount of $Cu_2O_{[200]}$. The reduced catalysts have a higher fraction

275 of $Cu_2O_{[200]}$.
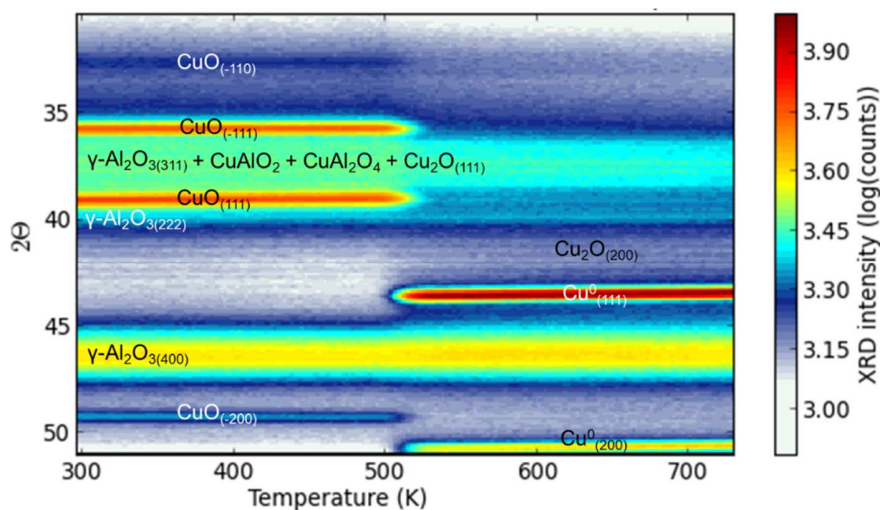
276

277 **Figure 3. Contour plots of the diffraction peaks as function of temperature between 32° and 52° during**
278 **reduction with 1.1 NmL s^{-1} 5 vol.% H$_2$-He of Cu oxides present in the 1.0La-10Cu catalyst.**

279 The material's morphology was further investigated *via* STEM. In calcined (Figure SI.3) and reduced

280 (Figure 4) samples of the 10Cu and 1.0La-10Cu catalysts, the porous structure was visible[69, 70],

281 while for the 1.0La-10Cu even the presence of cylindrical channels, as evidenced by N_2-sorption, was

282 observed. For both catalysts, it is clear that La and Cu remain highly dispersed over the $γ$-Al_2O_3

283 support. (Figure 4E and F) after reduction. For the 2.0La-10Cu catalyst (Figure SI.4), a catalyst grain

284 with larger Cu particles was found, however, the number was too small to obtain a particle size

285 distribution. In most images, no well-defined Cu-particles were identified, leading to the hypothesis

286 that most Cu particles are highly dispersed nanoparticles. The presence of a few larger Cu particles

287 is in agreement with the Cu^0 crystallites detected by XRD (Table SI.4).

288
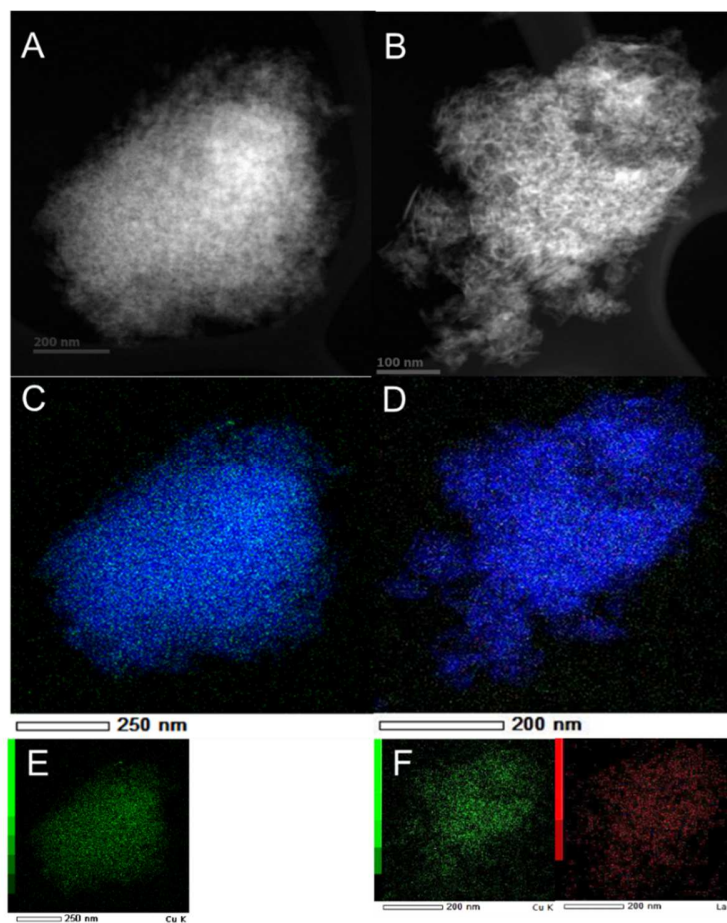
Figure 4. Dark-field STEM image of 10Cu (A) and 1.0La-10Cu (B) ex-situ reduced at 723 K using 10 vol.% H$_2$-Ar. The corresponding EDX elemental map with the distribution of Al (blue), Cu (green) and La (red) is shown in C and D. The individual EDX maps of Cu and La are shown in E, corresponding to the dark-field image A, and in F, corresponding to the dark-field image B.

3.1.3 Active sites related properties

As Cu^0 is needed for the hydrogenation reaction to achieve 1,2-propanediol, the catalysts have to be reduced prior to reaction. Hence, a more elaborate characterization of the reduced catalysts is needed to gain insights into the catalyst's surface and the role of Cu^0.

The mean surface area of the Cu aggregates, MSA$_{Cu^0}$, and the average diameter of the aggregates, $\emptyset_{Cu^0}$ in the reduced catalysts were determined *via* N$_2$O adsorption. The MSA$_{Cu^0}$ was found to be between 17 and 34 m² g$^{-1}_{cat}$, which is on the higher side of the range reported for typical supported

300 Cu-based catalysts in literature with similar Cu loading (10-30 m² g^{-1}_{cat}).[71-73] The average

301 diameter, $\emptyset_{Cu^0}$, increases with the Cu loading (Figures SI.5A). This is expected, since a higher Cu

302 loading enhances the probability of agglomeration and/or growth of the Cu particles during

303 synthesis.[74] The catalysts exhibited a dispersion, D_{Cu^0}, between 4 % and 20 %. The dispersion

304 decreases with increasing Cu loading (Figure SI.6B), as it is inversely related to $\emptyset_{Cu^0}$, see Table SI.4.

305   The acidity of the reduced catalysts was compared with that of the bare support, see Figure 5. The

306 addition of Cu resulted in a slight increase of the total acidity (Table SI.5). Compared to the calcined

307 support, the addition of Cu resulted to the formation of weak and strong acid sites (Figure 5A).

308 Moreover, it is clear that the interaction between La and Cu resulted in a different NH_3-TPD profile

309 compared to that obtained for the Cu-only catalyst. All La-promoted catalysts exhibited a significant

310 increase in the signal in the weak-moderate acid site region, compared to the support, and a lower

311 signal in the region of the strong acid sites.

312   The effect of the promotor ratio on the distribution of acid site types in the catalyst is depicted in

313 Figure 5E. Promotion slightly increased the fraction of weak-moderate acid sites and decreased the

314 number of strong acid sites. Lee *et al.*[75] reported that a higher La content decreased the strong

315 acidity in zeolites, due to the preferential interaction between La and strong acid hydroxyl groups

316 on the surface. XPS (*vide infra*) showed an increased amount of surface Cu^+, which correspond to

317 Lewis acidity species because of the electron affinity [19, 21, 28, 76-79], upon La-promotion (Figure

318 SI.10B). It was possible to estimate the distribution of the acid sites induced by the Cu^+ (Table SI.5).
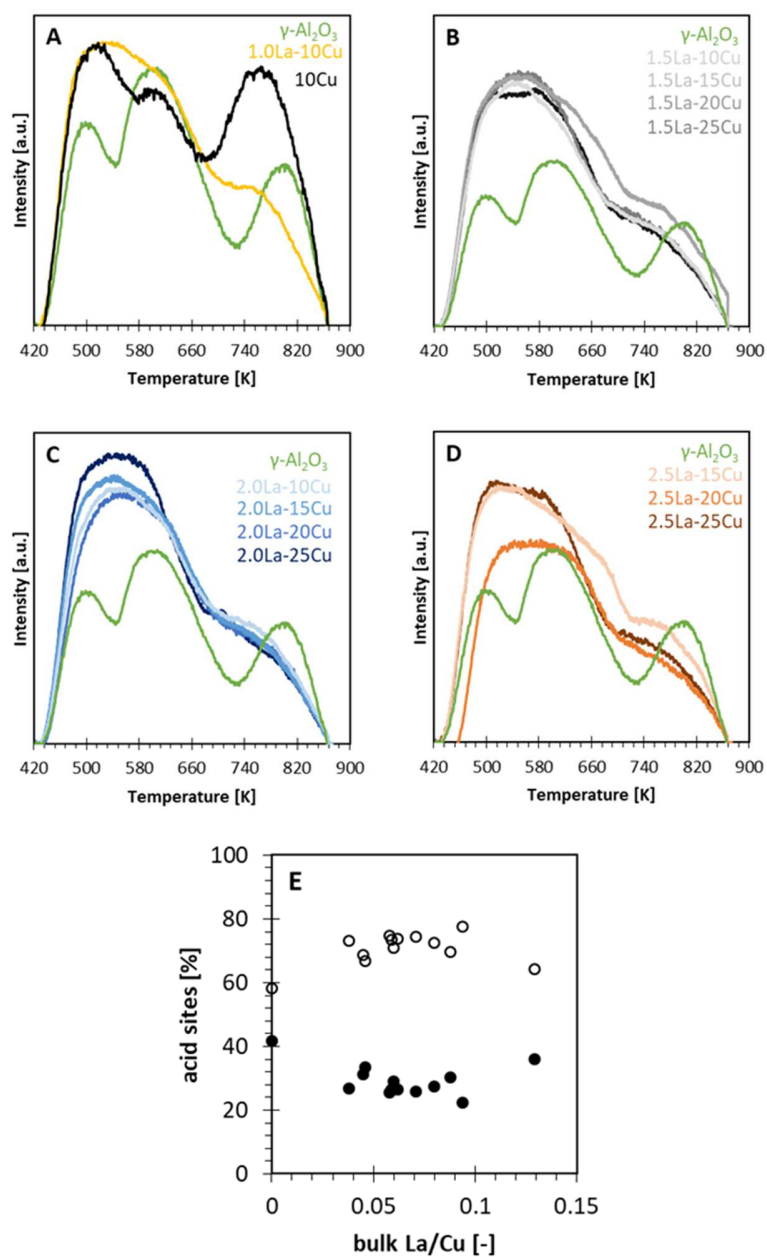
Figure 5. NH$_3$-TPD profiles of the calcined support (green) and (A): 10Cu (black), 1.0La-10Cu (yellow); (B): 1.5La-yCu; (C): 2.0La-yCu and (D): 2.5La-yCu catalysts. Intensities were normalized per support mass, such that additional acidity generated by metal deposition can be visually identified. (E) Effect of the bulk La/Cu mass ratio on the fraction of amount of weak-moderate (○) and strong (●) acid sites, as determined by NH$_3$-TPD.

3.1.4 Overall reduction behavior

The effect of promotion on the Cu species of the calcined catalysts and their reduction behavior was investigated by H_2-TPR, of which the reduction profiles are shown in Figure 6. This analysis provides insight into the overall surface species and catalyst reducibility, while an XRD measurement (section 3.1.2) provides only information about the reduction of crystalline phases. It can be clearly seen that the addition of La to the 10Cu catalyst (Figure 6A) decreased the intensity of the α peak, while that of the β peak increased. The first reduction peak, α, might be ascribed to highly dispersed CuO species[80] and/or $(Cu-O-Cu)^{2+}$ species[47], the second reduction peak, β, to the reduction of CuO particles with weak support interactions[81, 82]. The 1.0La-10Cu catalyst did not show any bulk CuO, corresponding to the γ-peak[80-82], but had a higher number of CuO particles with strong support interactions[81, 82], corresponding to β'. This species could correspond to the $CuAl_2O_4$ crystallites which were not clearly detectable with XRD in section 3.1.2. For the other catalysts (Figure 6B to D), three main reduction peaks were distinguished. At higher Cu-loadings, the reduction peaks shifted to higher temperature. The reduction peak γ increased with higher Cu-loading, as a result of larger Cu particles, see Table SI.4. For all catalysts, the hydrogen consumption during H_2-TPR was somewhat lower than the stoichiometric value for complete reduction from CuO to Cu^0, resulting in a degree of reduction between 76 % and 98 % (Table SI.4). Most likely, the remaining amount of non-reduced $Cu^{\delta+}$ species have a stronger interaction with the support, such as $CuAlO_2$ or Cu_2O. This value related to the amount of Cu^{2+} in the calcined sample is in agreement with the determined amount of Cu^{2+} on the calcined catalysts by XPS (Table SI.6). In short, it is plausible that in addition to Cu^0 species, a lower amount of $Cu^{\delta+}$ species remains present after reduction, as also indicated by the *in situ* XRD in Figure 3.
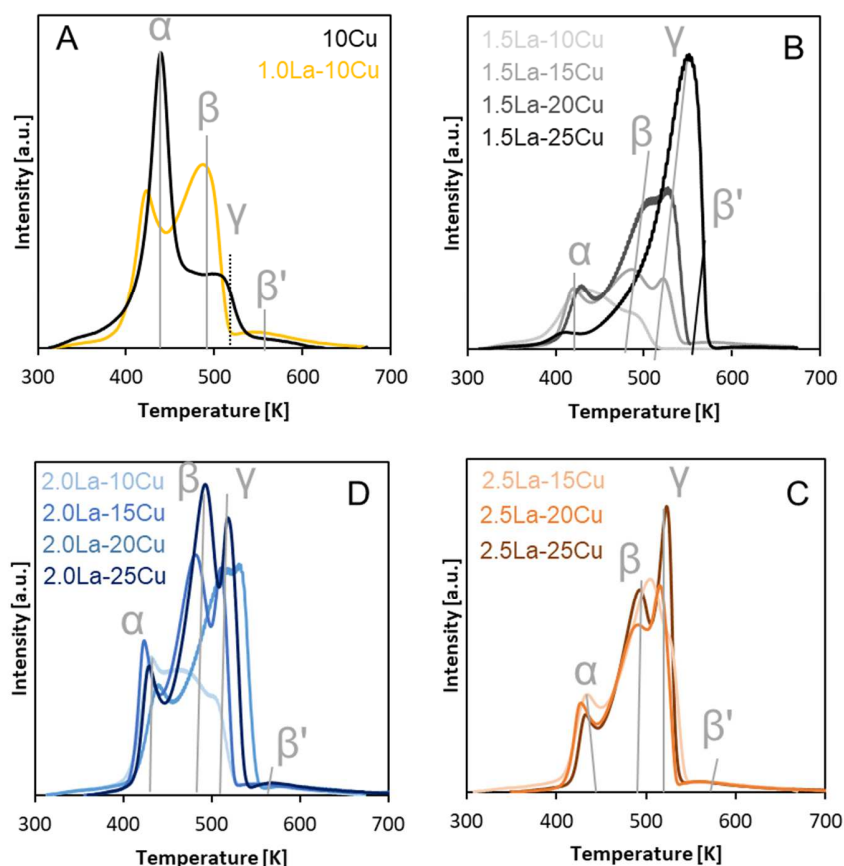
Figure 6. TPR profiles of the calcined catalysts with (A): 10Cu (black), 1.0La-10Cu (yellow); (B): 1.5La-yCu;
(C): 2.0La-yCu and (D): 2.5La-yCu.

3.1.5 Identification of the surface species

The effect of the promotion on the chemical surface composition and oxidation states in the
calcined and reduced La-Cu catalysts was analyzed *via* XPS. Being a surface technique, the
representativeness of the results to the whole catalyst should be verified by comparing the La/Al
and Cu/Al mass ratios, in the calcined catalysts, determined by XPS (surface composition) to those
determined by ICP (bulk composition), see Table SI.3. Note that the La surface composition almost
corresponds to that of the bulk, even though Cu is deposited after La (Figure SI.8A). For all calcined
catalysts, the low Cu/Al ratios in XPS clearly indicate that quite some Cu is present as bulk Cu, rather

358   than being exposed at the surface (Figure SI.8B). The photoelectron peaks at 932.6 eV were assigned

359   to the binding energy (BE) of Cu $2p_{3/2}$, as illustrated in Figure 7. The presence of a pronounced

360   satellite peak between 942 eV and 948 eV was ascribed to a contribution by Cu^{2+}. Due to the

361   asymmetry of the Cu $2p_{3/2}$ peak, the Cu^{2+} species in the calcined catalysts are ascribed to CuO (933.5

362   eV) and $CuAl_2O_4$ (935 eV).[83] The latter is apparently in contrast with the XRD diffraction pattern

363   (section 3.1.2). However, XPS being a surface analysis technique, this can be interpreted as a

364   difference between the surface and bulk composition. When comparing the Cu $2p_{3/2}$ BE of the

365   Cu-only calcined catalysts to the La-Cu catalysts, a shift to lower BE was observed (Figure SI.9A, Table

366   SI.6). This may indicate that as La is added first, the Cu particles are preferentially located next to

367   the La particles rather than covering them, as the bulk La/Al corresponded well with the surface

368   La/Al ratio (Figure SI.8A). The shift to lower BE for Cu $2p_{3/2}$ points to the overlap of the d-orbitals of

369   La and Cu, indicating a strong La-Cu interaction.[84] The latter can lead to the formation of Cu

370   species with a lower oxidation state, such as Cu^+, which is in agreement with the observations by in

371   situ XRD (Figure 3). As such, the relative amount of Cu^{2+} in the calcined catalysts decreases with the

372   percentage of surface La and varies between 100 % and 80 % (Figure SI.9B, Table SI.6).
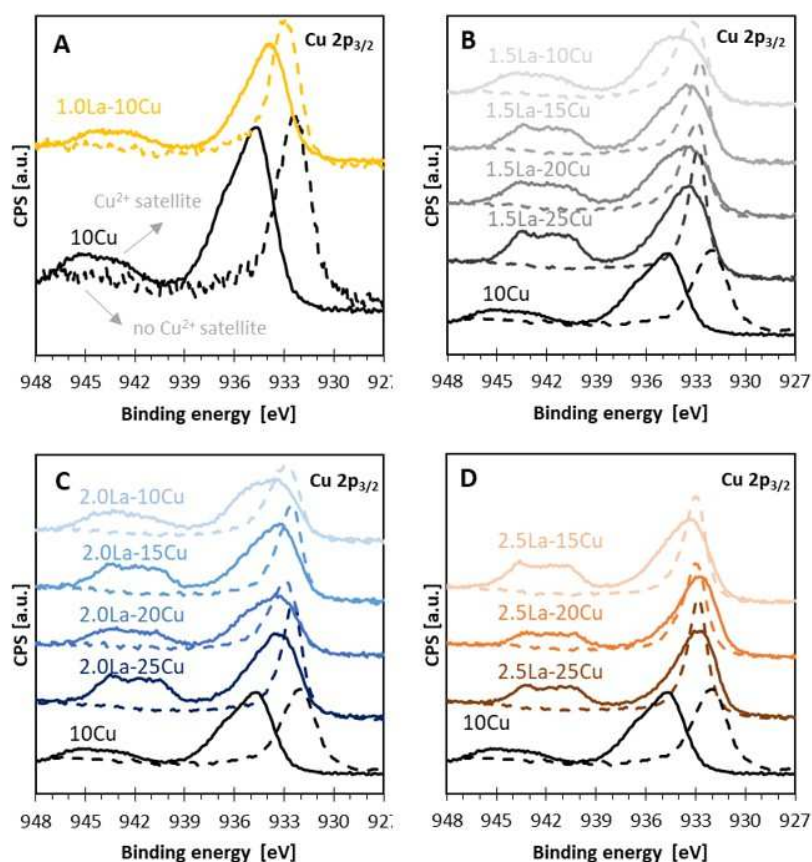
Figure 7. Cu 2p3/2 spectra of calcined (full line) and reduced (dashed line) 10Cu catalyst (black) and (A): 1.0La-10Cu (yellow); (B): 1.5La-yCu; (C): 2.0La-yCu and (D): 2.5La-yCu.

For the reduced catalysts, the Cu/Al ratio decreased approximately 50 % compared to the calcined samples (Table SI.7, *cf.* Table SI.*6*). As the reduction temperature is not sufficiently high to allow the diffusion of Cu into the Al_2O_3 structure[27, 85], this indicates a lower dispersion (and, hence, sintering) of the Cu particles. This is in agreement with the change in Cu crystallite size observed by XRD (Table SI.4, *cf.* Table SI.3). There was no satellite peak between 942 and 944 eV ascribed to Cu^{2+}, implying reduction of Cu^{2+} to Cu^+ and/or Cu^0 (Figure 7). Comparing the calcined to the reduced catalysts (Table SI.6, *cf.* Table SI.7), a shift to lower BE was observed for all catalysts. The largest shift, from 934.6 eV (Cu^{2+}) to 932.3 eV (Cu^0), was observed for the unpromoted Cu catalyst, while the La-Cu catalysts showed a smaller shifts, due to the strong interaction between La and Cu. One

22

385 can presume that the larger shift for the unpromoted Cu catalysts is either to the larger particle size

386 or less Cu^+.

387 Due to the similar BE between Cu^+ (932.2 ± 0.1 eV) and Cu^0 (932.6 ± 0.3 eV), it is hard to

388 discriminate between those Cu species.[86] To clearly distinguish between Cu^+ and Cu^0 in the

389 reduced catalysts, a deep analysis of the Auger Cu LMM region was performed. The Cu LMM

390 spectrum shows larger differences (1.8 eV) between the kinetic energy (KE) of the Cu species

391 compared to the BE. As shown in Figure 8, the Cu LMM spectra of the reduced La-Cu catalysts

392 present an asymmetrical broad peak, suggesting the coexistence of Cu^+ and Cu^0 on the catalysts

393 surface.[86] The higher the Cu loading, the more pronounced the Cu^0 and Cu^+ peaks are. Even if the

394 intensity of the Auger peaks is low, the concentration of the individual species could be determined

395 by the use of Cu standards. Notwithstanding that, caution is needed when interpreting the results

396 as small shifts in KE could result in different fractions of Cu^0 and Cu^+. When looking carefully at the

397 individual Cu^0 and Cu^+ species present on the surface of the reduced catalysts, the strong La-Cu

398 interaction is again noticeable. The higher the La/Cu surface mass ratio, the higher the percentage

399 of Cu^+ species remained present after the reduction (*vide supra*, Figure SI.10). The values are

400 summarized in Table SI.7. It was also evidenced by the Wagner plot[86] that the surface of the

401 reduced La-Cu catalysts is covered with Cu^+ rather than with Cu^0 (Figure SI.11). Only the bare Cu

402 catalyst showed more Cu^0 than Cu^+ on the reduced catalyst surface.
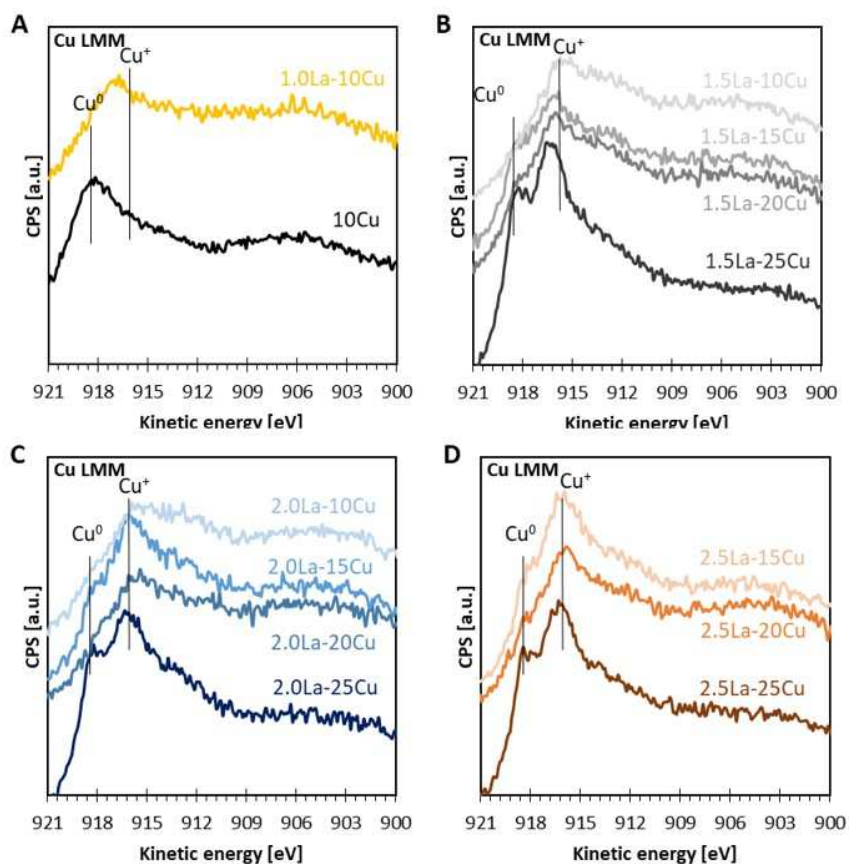
Figure 8. Cu LMM spectra of the catalysts after reduction at 623 K using 100 %H$_2$ at 0.33 NmL s^{-1}.
(A): 10Cu (black), 1.0La-10Cu (yellow); (B): 1.5La-yCu; (C): 2.0La-1yCu and (D): 2.5La-yCu.

In summary, the La promotion has no pronounced effect on the textural properties of the calcined catalysts. The calcined catalysts exhibit a homogenous distribution of dispersed La and Cu particles. The La-Cu interaction resulted in Cu species with lower oxidation states, but the major part of the species remained in the Cu^{2+} oxidation state on the calcined catalysts. After reduction, the Cu agglomerates remain well dispersed and the dispersion of Cu^0 on the reduced catalysts decreases with increasing Cu loading. Most of the Cu^0 particles sizes are between 1-10 nm while some larger bulk Cu^0 crystallites are also present. Due to the important La-Cu interaction, a significant amount of non-reduced Cu$^+$ species remains present after the reduction – most probably at the surface of

24

414   the Cu^0 particles – whereby, the acidity of the catalysts also slightly increases, as Cu^+ species are

415   considered as moderate (Lewis) acids.

416   **3.2   Glycerol hydrogenolysis**

417   To investigate the effect of La/Cu mass ratio on the catalytic performance, *i.e.* the catalyst's

418   stability, activity and selectivity, five La-Cu catalysts were selected and compared to the 10Cu

419   catalyst. A La-Cu catalyst with the similar MSA_{Cu^0} as the 10Cu catalyst but different Cu particle sizes,

420   *i.e.* 1.5La-20Cu was selected. The 1.0La-10Cu and 2.0La-20Cu catalysts were also selected as those

421   exhibited the same promoter ratio, however, with different Cu particles. Finally, the La-Cu catalysts

422   with respectively the highest and lowest MSA_{Cu^0}, *i.e.* 1.5La-10Cu and 2.0La-10Cu, were also

423   selected.

424   **3.2.1   Catalytic performance**

425   Figure 9A shows the effect of the La/Cu mass ratio on the catalyst stability, expressed as the

426   relative decrease in glycerol conversion over 68 h TOS (Table SI.8 till Table SI.13). It is clear that La-

427   Cu catalyst exhibited a better catalyst stability compared to the pure Cu catalyst. The increased

428   stability was attributed the a lower amount of sintering (vide supra, section 3.2.2).

429   The effect of the promotion on the catalyst activity is shown in Figure 9B. La-promotion did not

430   increase the activity, in agreement with our previous work[38]. For a constant MSA_{Cu^0}, the activity

431   even rather decreases upon La 'promotion'. This indicates that a tradeoff will be needed between

432   stability and activity. The pure Cu catalyst has a higher activity even though no acidic Cu^+ is present

433   on the surface (Table SI.7). However, a small acid contribution of Cu was estimated (Figure 9D),

434   which could be the result of some $Cu-Al_2O_3$ interactions. Therefore, it seems that the active sites on

435   the pure Cu and the La-Cu catalysts are different.

436

437

438
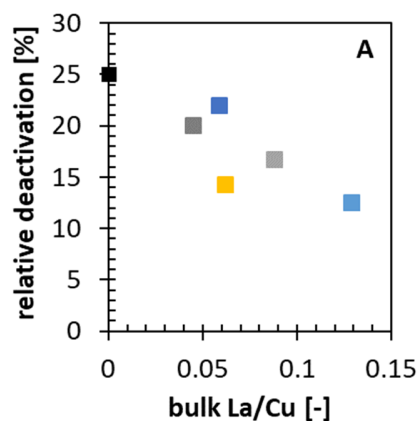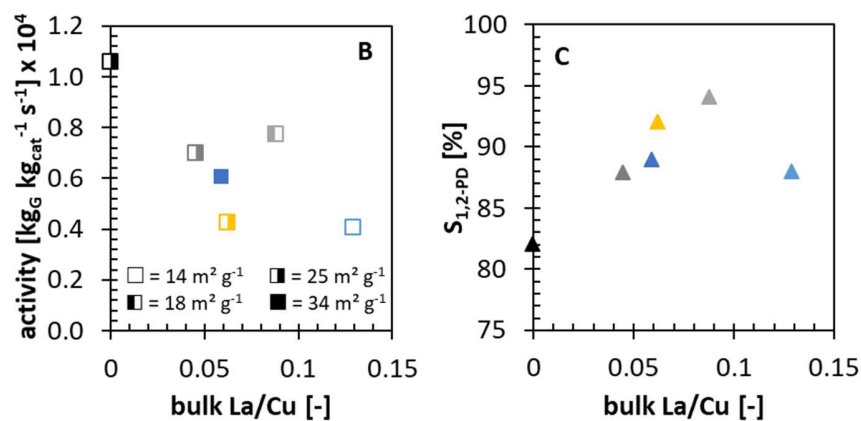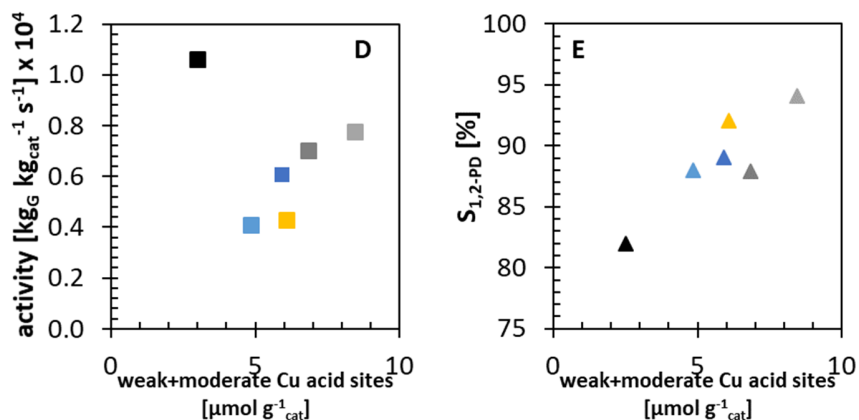
Figure 9. Effect of bulk La/Cu mass ratio on (A) the stability, (B) activity and (C) 1,2-propanediol
selectivity. Effect of the weak and moderate Cu acid sites on (D) the activity and (E) 1,2-propanediol
selectivity. Activity and selectivity are determined after 12 h time on stream at 125 kg$_{cat}$ s mol$^{-1}_{glycerol}$, 473
K, a total H$_2$ pressure of 7.5 MPa and a molar H$_2$ to glycerol ratio of 7 for the 10Cu (black), 1.5La-20Cu
(dark grey), 2.0La-20Cu (dark blue), 1.0La-10Cu (yellow), 1.5La-10Cu (light grey) and 2.0La-10Cu (light
blue).

439
440
441
442
443
444

26

445   The 1,2-propanediol selectivity seemed to increase up to a La/Cu mass ratio of 0.088 (*i.e.* the 1.5La-

446   10Cu catalyst), see Figure 9C. The 2.0La-10Cu catalyst, which has the largest La/Cu mass ratio,

447   showed a lower 1,2-propanediol selectivity. The latter has almost the same total acidity compared

448   to the 1.5La-10Cu catalyst (Table SI.5) but exhibited different acid site distribution (Figure 5E). To

449   better understand this effect, Figure 9E depicts selectivity as a function acid sites introduced by the

450   Cu loading, i.e. the concentration of weak and moderate sites that exceed the ones of the bare

451   support (Table SI.5). It is clear that the increasing number of weak-moderate Cu acid sites

452   contributes to the increase in selectivity, where that is not the case for the support acid sites (Figure

453   SI.11A). It seems that the main difference between a pure Cu/Al_2O_3 and the $La-Cu/Al_2O_3$ catalysts is

454   attributed to the Lewis acidity of Cu^+, as results of the La-Cu interactions. The weak-moderate Cu^+

455   acid sites in La-Cu catalysts, enhanced glycerol conversion to acetol (Figure SI.11B), which is the rate

456   determining step[46], and consequently resulted in higher 1,2-propanediol selectivity.

457   A minor amount of 1,3-propanediol or degradation products, such as 1-propanol and 2-propanol,

458   were also observed over some catalysts (Table SI.8 till Table SI.13). For all catalysts, the undesired

459   C-C cleavage, forming 1,2-ethanediol was observed. The selectivity of 1,2-ethanediol was not

460   directly related to the number of strong acid sites (Figure SI.11C), which are generally assumed to

461   promote C-C cleavage. This could be related to the low selectivity towards the product and a higher

462   experimental error. However, the La-Cu catalysts exhibited an increase in 1,2-ethanediol selectivity

463   with increasing total number of acid sites per Cu^0 site (Figure SI.11D). This indicates that for the

464   direct hydrogenolysis of glycerol to 1,2-ethanediol and methanol both an acid and a metal site are

465   required, rather than only a metal site.

466

3.2.2 Spent catalyst characterization

During reaction, the catalyst can undergo changes in particle size, oxidation state and morphology. Therefore, the six investigated catalysts were also thoroughly characterized *post* reaction (68 h TOS). The La-Cu catalysts are not subject to leaching (Table SI.14 *cf.* Table SI.2). From the XRD patterns of the spent catalysts, shown in Figure 10, one can see that the CuO signal reappeared, especially in the case of the 10Cu catalyst. This indicates that some amount of the Cu species reoxidized or some CuO sintered during the reaction. Further, it can be observed that the diffraction peaks of Cu^0 are very sharp, indicating larger crystallite sizes.
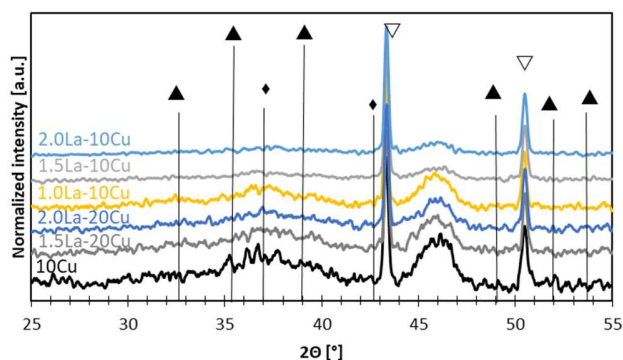
Figure 10. XRD pattern of the spent 10Cu (black), 1.5La-20Cu (dark grey), 2.0La-20Cu (dark blue), 1.0La-10Cu (yellow), 1.5La-10Cu (light grey) and 2.0La-10Cu (light blue) catalyst with CuO (▲), Cu_2O (♦) and Cu^0 (▽).

Based on the Scherrer equation, Cu^0 crystallites in the range of 50 to 150 nm were observed on the spent catalyst, see Figure 11, but this size decreased with increasing La/Cu mass ratio. This trend was also confirmed by dissociative N_2O adsorption on the spent catalysts. To investigate the morphology of the spent catalysts, STEM images of the spent catalysts, without any pretreatment, were made and a particle size distribution was determined (Figure SI.12). Based on dark-field STEM, the stabilizing effect of La was evident. The effect of the promotor ratio was less straightforward to interpret (Figure 11) as compared to other characterization method. Thus, La-promotion inhibited

486   sintering of not only Cu^0, but of all Cu species in the catalyst as it is impossible to distinguish different

487   oxidation states in STEM. As discussed in section 3.1.4, the La-Cu interactions also increased the

488   amount of Cu^+ species, reducing again the extent of Cu species sintering.
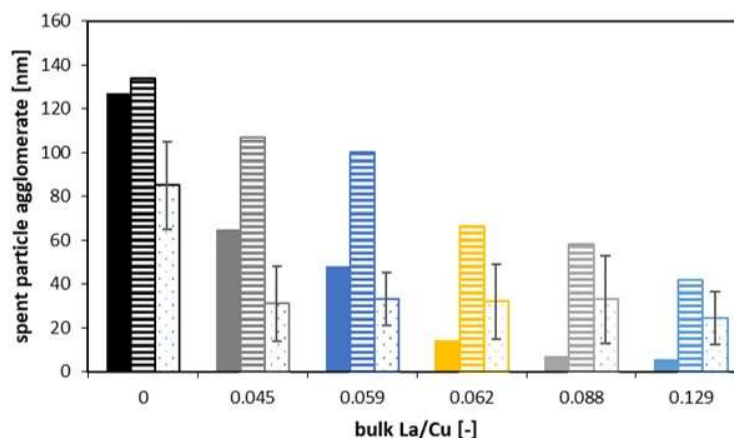
489

490   **Figure 11. Effect of La/Cu mass ratio on the spent Cu particle size, d_{Cu^0}, determined by dissociative N_2O**
491   **adsorption (full bars), Scherrer equation (striped bars) and STEM (dotted bars) of 10Cu (black), 1.5La-20Cu**
492   **(dark grey), 2.0La-20Cu (dark blue), 1.0La-10Cu (yellow), 1.5La-10Cu (light grey) and 2.0La-10Cu (light blue)**
493   **catalyst.**

494   Figure 12 shows the dark-field STEM images of the spent 10Cu and spent 1.0La-10Cu catalyst.

495   Whereas in the calcined (Figure SI.3) and reduced catalysts (Figure 4), Cu was highly dispersed, there

496   is a clear presence of large Cu particles after reaction. Notwithstanding that, a population of highly

497   dispersed Cu was still present, see Figure 15F. For the unpromoted catalyst, larger agglomerates

498   were observed (taking notice to the difference in scale between Figure 15E and F), while for the La-

499   Cu catalysts the majority of the Cu particles form agglomerates of *ca.* 20-30 nm (see Figure SI.12).
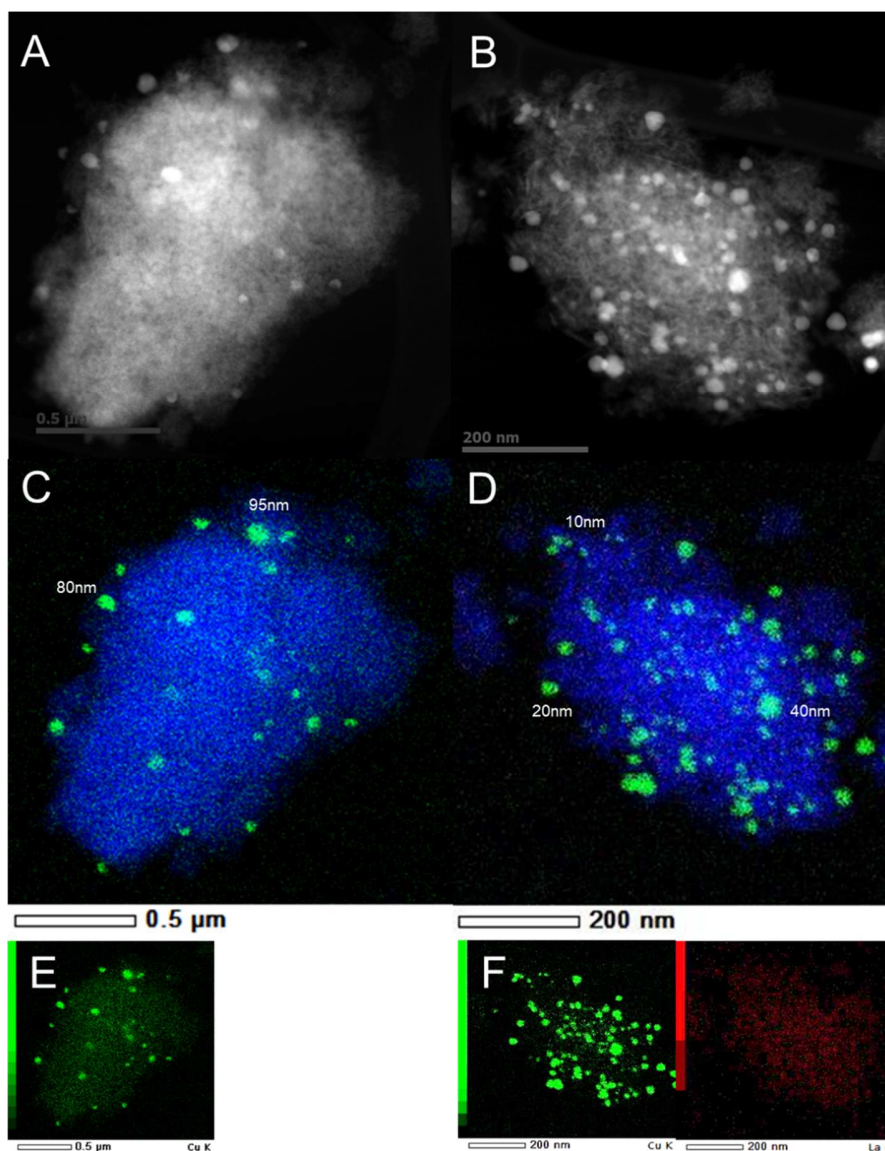
Figure 12. Dark-field STEM image of spent 10Cu (A) and 1.0La-10Cu (B) catalyst. The corresponding EDX elemental map with the distribution of Al (blue), Cu (green) and La (red) is shown in C and D. The individual EDX maps of Cu and La are shown in E, corresponding to the dark-field image A, and in F, corresponding to the dark-field image B.

The surface state of the spent Cu and La-Cu catalysts was probed by XPS. A small satellite peak between 942 and 944 eV was detected and ascribed to Cu^{2+}, see Figure SI.13, implying some reoxidation compared to the reduced catalysts, as was observed with XRD (Figure 10). The percentage of (Cu^0+Cu^+) present in the spent catalysts (Figure SI.14), increased with the La/Cu mass

509   ratio. Due to the strong La-Cu interactions, it was assumed that Cu^+ was present on the surface of

510   the reduced catalyst, as discussed in section 3.1.5, and remained in the spent catalysts.

511   It is concluded that the La-Cu catalysts showed a better stability (see Figure 9A) as result of the

512   strong La-Cu interactions, which reduced the extent of Cu sintering.

513   **3.3   Proposed reaction mechanism over La-Cu/γ-Al$_2$O$_3$ catalysts**

514   As mentioned in the introduction, the most accepted mechanism for the formation of 1,2-

515   propanediol is the dehydration-hydrogenation one. In the first step, glycerol is dehydrated over an

516   acid site, induced by the support, to acetol, while in the second step, these intermediates undergo

517   hydrogenation, which is catalyzed by a metallic site, to 1,2-propanediol. Combining the observed

518   characteristics and catalytic performance, our work allows to propose a more specific mechanism

519   for glycerol hydrogenolysis over La-Cu/γ-Al$_2$O$_3$. This mechanism, hypothesizes that Cu particles,

520   rather than the support, are the active sites for the dehydration to acetol. Figure 13 illustrates the

521   role of the different surface Cu species in this reaction mechanism.

522   As evidenced by STEM, both the La and Cu agglomerates are well dispersed in the reduced

523   catalysts. The Cu-loading affected mostly the size of the Cu^0 particles (1.3 – 5.5 nm). XPS indicated

524   the co-existence of Cu^0 and Cu^+, as represented in Figure 14. At higher La/Cu mass ratios, more Cu^+

525   is available on the surface.
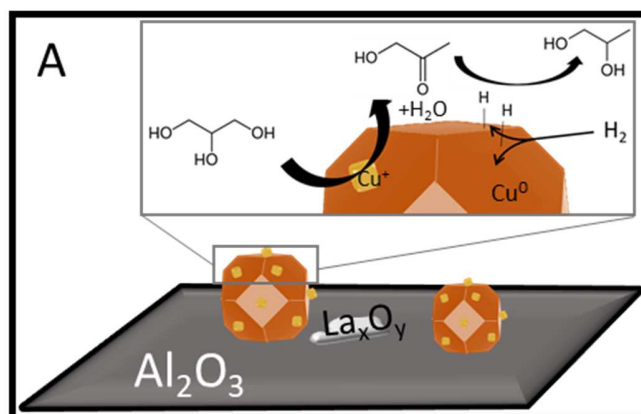
Figure 13. Schematic representation of proposed role of La-Cu/γ-Al₂O₃ in glycerol hydrogenolysis. (A) La-Cu/γ-Al₂O₃ surface and the interaction between Cu⁺ and Cu⁰ in 1,2-propanediol formation.

As shown in Figure 13, H_2 adsorbs dissociative on any Cu^0 surface with the formation of two adsorbed hydrogen atoms. The adsorption of glycerol then occurs on Cu^+, induced by the La-Cu interaction. It is assumed, inspired by the mechanism proposed by Alhanash *et al.*[39], that a primary hydroxyl group of glycerol interacts with the Cu^+, which has Lewis acidity, and an O atom of Cu_2O abstracts a proton on the adjacent carbon. Cu^+ weakens the electron density of the C-O bond[28, 87], accelerating its cleavage; yielding acetol and water by regeneration of the active site (dehydration). Finally, acetol reacts with two of the hydrogen atoms on the Cu^0 surface, leading to the formation of 1,2-propanediol. An acid site in the proximity of a Cu^0 site contributed to side product formation.

4 Conclusions

In this work, the effect of La-promotion on γ-Al₂O₃ supported Cu catalyst for glycerol hydrogenolysis towards 1,2-propanediol was assessed. Different promoter ratios were employed, leading to varying amounts of Cu^+ and Cu^0 species.

542   The La/Cu mass ratio had no significant effect on the textural properties (*e.g.* surface area, average

543   pore size and pore volume) of the calcined catalysts. After the reduction of the catalysts, Cu^+ and

544   Cu^0 co-existed. It was found that La/Cu mass ratio, affected the amount of Cu^+ and consequently the

545   acid site distribution.

546   The activity seemingly decreased with promotion ratio, causing a tradeoff between stability and

547   activity. Sintering of the Cu particles occurred, but its extent was reduced by the presence of La

548   thanks to the La-Cu interaction. It was shown that product selectivity in glycerol hydrogenolysis on

549   La-Cu/Al$_2$O$_3$ catalysts depends on both acid and metal sites. The weak-moderate Cu^+ acid sites in La-

550   Cu catalysts, rather than the support, enhanced the dehydration of acetol, and consequently to the

551   1,2-propandiol selectivity. The insights gained in this work provide a new view on the role of Cu^+ and

552   therefore the complexity of glycerol hydrogenolysis. Additional *operando* characterization could

553   provide fundamental understanding of the glycerol conversion and facilitating rational catalyst

554   design.

560 **References**

561 [1] A. Behr, The Future of Glycerol. New Usages for a Versatile Raw Material. By Mario Pagliaro and
562 Michele Rossi, ChemSusChem, 1 (2008) 653-653.

563 [2] F. Bauer, C. Hulteberg, Is there a future in glycerol as a feedstock in the production of biofuels
564 and biochemicals?, Biofuels, Bioproducts and Biorefining, 7 (2013) 43-51.

565 [3] M. Pagliaro, M. Rossi, Glycerol: properties and production, The future of glycerol, Society of
566 Chemistry2010.

567 [4] R. Ciriminna, C.D. Pina, M. Rossi, M. Pagliaro, Understanding the glycerol market, European
568 Journal of Lipid Science and Technology, 116 (2014) 1432-1439.

569 [5] C.-H.C. Zhou, J.N. Beltramini, Y.-X. Fan, G.M. Lu, Chemoselective catalytic conversion of glycerol
570 as a biorenewable source to valuable commodity chemicals, Chemical Society Reviews, 37 (2008)
571 527-549.

572 [6] M. Sara, T. Rouissi, S.K. Brar, J.F. Blais, Chapter 5 - Propylene Glycol: An Industrially Important
573 C3 Platform Chemical, in: S. Kaur Brar, S. Jyoti Sarma, K. Pakshirajan (Eds.) Platform Chemical
574 Biorefinery, Elsevier, Amsterdam, 2016, pp. 77-100.

575 [7] M.R. Nanda, Z. Yuan, W. Qin, C. Xu, Recent advancements in catalytic conversion of glycerol into
576 propylene glycol: A review, Catalysis Reviews, 58 (2016) 309-336.

577 [8] Y. Wang, J. Zhou, X. Guo, Catalytic hydrogenolysis of glycerol to propanediols: a review, RSC
578 Advances, 5 (2015) 74611-74628.

579 [9] M.A. Dasari, P.-P. Kiatsimkul, W.R. Sutterlin, G.J. Suppes, Low-pressure hydrogenolysis of
580 glycerol to propylene glycol, Applied Catalysis A: General, 281 (2005) 225-231.

581 [10] Z. Ma, Z. Xiao, J.A. van Bokhoven, C. Liang, A non-alkoxide sol–gel route to highly active and
582 selective Cu–Cr catalysts for glycerol conversion, Journal of Materials Chemistry, 20 (2010) 755-760.

583 [11] Z. Xiao, X. Wang, J. Xiu, Y. Wang, C.T. Williams, C. Liang, Synergetic effect between Cu0 and
584 Cu+ in the Cu-Cr catalysts for hydrogenolysis of glycerol, Catalysis Today, 234 (2014) 200-207.

585 [12] A. Bienholz, F. Schwab, P. Claus, Hydrogenolysis of glycerol over a highly active CuO/ZnO
586 catalyst prepared by an oxalate gel method: influence of solvent and reaction temperature on catalyst
587 deactivation, Green Chemistry, 12 (2010) 290-295.

588 [13] M. Balaraju, V. Rekha, P.S. Sai Prasad, R.B.N. Prasad, N. Lingaiah, Selective Hydrogenolysis
589 of Glycerol to 1, 2 Propanediol Over Cu–ZnO Catalysts, Catal Lett, 126 (2008) 119-124.

590 [14] S. Wang, H. Liu, Selective hydrogenolysis of glycerol to propylene glycol on Cu–ZnO catalysts,
591 Catal Lett, 117 (2007) 62-67.

592 [15] M. Balaraju, K. Jagadeeswaraiah, P.S.S. Prasad, N. Lingaiah, Catalytic hydrogenolysis of
593 biodiesel derived glycerol to 1,2-propanediol over Cu-MgO catalysts, Catalysis Science &
594 Technology, 2 (2012) 1967-1976.

595 [16] Z. Yuan, J. Wang, L. Wang, W. Xie, P. Chen, Z. Hou, X. Zheng, Biodiesel derived glycerol
596 hydrogenolysis to 1, 2-propanediol on Cu/MgO catalysts, Bioresource technology, 101 (2010) 7088-
597 7092.

598 [17] Z. Yuan, L. Wang, J. Wang, S. Xia, P. Chen, Z. Hou, X. Zheng, Hydrogenolysis of glycerol over
599 homogenously dispersed copper on solid base catalysts, Applied Catalysis B: Environmental, 101
600 (2011) 431-440.

601 [18] A. Bienholz, H. Hofmann, P. Claus, Selective hydrogenolysis of glycerol over copper catalysts
602 both in liquid and vapour phase: Correlation between the copper surface area and the catalyst's
603 activity, Applied Catalysis A: General, 391 (2011) 153-157.

604 [19] J. Shan, H. Liu, K. Lu, S. Zhu, J. Li, J. Wang, W. Fan, Identification of the dehydration active sites
605 in glycerol hydrogenolysis to 1,2-propanediol over Cu/SiO2 catalysts, Journal of Catalysis, 383 (2020)
606 13-23.

607 [20] E.S. Vasiliadou, T.M. Eggenhuisen, P. Munnik, P.E. de Jongh, K.P. de Jong, A.A. Lemonidou,
608 Synthesis and performance of highly dispersed Cu/SiO2 catalysts for the hydrogenolysis of glycerol,
609 Applied Catalysis B: Environmental, 145 (2014) 108-119.

610 [21] S. Zhu, X. Gao, Y. Zhu, W. Fan, J. Wang, Y. Li, A highly efficient and robust Cu/SiO2 catalyst
611 prepared by the ammonia evaporation hydrothermal method for glycerol hydrogenolysis to 1,2-
612 propanediol, Catalysis Science & Technology, 5 (2015) 1169-1180.

613 [22] Z. Wu, Y. Mao, M. Song, X. Yin, M. Zhang, Cu/boehmite: A highly active catalyst for
614 hydrogenolysis of glycerol to 1,2-propanediol, Catalysis Communications, 32 (2013) 52-57.

615 [23] M.L. Dieuzeide, M. Jobbagy, N. Amadeo, Vapor-Phase Hydrogenolysis of Glycerol to 1,2-
616 Propanediol over Cu/Al2O3 Catalyst at Ambient Hydrogen Pressure, Industrial & Engineering
617 Chemistry Research, 55 (2016) 2527-2533.

618 [24] I. Gandarias, J. Requies, P.L. Arias, U. Armbruster, A. Martin, Liquid-phase glycerol
619 hydrogenolysis by formic acid over Ni–Cu/Al2O3 catalysts, Journal of Catalysis, 290 (2012) 79-89.

620 [25] Y. Liu, N. Pasupulety, K. Gunda, G.L. Rempel, F.T. Ng, Glycerol Hydrogenolysis to 1, 2-
621 Propanediol by Cu/ZnO/Al2O3 Catalysts, Topics in Catalysis, 57 (2014) 1454-1462.

622 [26] D. Sun, Y. Yamada, S. Sato, Effect of Ag loading on Cu/Al2O3 catalyst in the production of 1,2-
623 propanediol from glycerol, Applied Catalysis A: General, 475 (2014) 63-68.

624 [27] F. Vila, M. López Granados, M. Ojeda, J.L.G. Fierro, R. Mariscal, Glycerol hydrogenolysis to 1,2-
625 propanediol with Cu/γ-Al2O3: Effect of the activation process, Catalysis Today, 187 (2012) 122-128.

626 [28] Q. Wang, Z. Yu, J. Feng, P. Fornasiero, Y. He, D. Li, Insight into the Effect of Dual Active Cu0/Cu+
627 Sites in a Cu/ZnO-Al2O3 Catalyst on 5-Hydroxylmethylfurfural Hydrodeoxygenation, ACS Sustain.
628 Chem. Eng., 8 (2020) 15288-15298.

629 [29] A. Wolosiak-Hnat, E. Milchert, B. Grzmil, Influence of Parameters on Glycerol Hydrogenolysis
630 over a Cu/Al2O3 Catalyst, Chemical Engineering & Technology, 36 (2013) 411-418.

631 [30] A. Wołosiak-Hnat, E. Milchert, G. Lewandowski, B. Grzmil, Influence of reduction time of copper
632 based catalysts: Cu/Al2O3 and CuCr2O4 on hydrogenolysis of glycerol, Polish Journal of Chemical
633 Technology, 13 (2011) 71-76.

634 [31] L.C. Meher, R. Gopinath, S.N. Naik, A.K. Dalai, Catalytic Hydrogenolysis of Glycerol to Propylene
635 Glycol over Mixed Oxides Derived from a Hydrotalcite-Type Precursor, Industrial & Engineering
636 Chemistry Research, 48 (2009) 1840-1846.

637 [32] X. Deng, Y.-J. Liu, W. Huang, Higher alcohols synthesis from syngas over lanthanum-promoted
638 CuZnAl catalyst, Journal of Energy Chemistry, 27 (2018) 319-325.

639 [33] R.B. Mane, A.M. Hengne, A.A. Ghalwadkar, S. Vijayanand, P.H. Mohite, H.S. Potdar, C.V. Rode,
640 Cu: Al nano catalyst for selective hydrogenolysis of glycerol to 1, 2-propanediol, Catal Lett, 135 (2010)
641 141-147.

642 [34] M.V. Twigg, M.S. Spencer, Deactivation of supported copper metal catalysts for hydrogenation
643 reactions, Applied Catalysis A: General, 212 (2001) 161-174.

644 [35] A.B. Miller, M. Raghunath, V. Sokolovskii, C.G. Lugmair, J. Anthony F. Volpe, W. Shen, W.
645 Turbeville, Catalyst for polyol hydrogenolysis, US20140249334A1, 2014.

646 [36] L. Zhiguo, G. Zhenmei, L. Pei, Z. Weiwei, Method for preparing propylene glycol by glycerin
647 hydrogenolysis, CN201210419541.9A, 2012.

648 [37] R.B. Mane, C.V. Rode, Effect of Cometals in Copper Catalysts for hydrogenolysis of Glycerol to
649 1, 2-Propanediol, Biomass and Biofuels: Advanced Biorefineries for Sustainable Production and
650 Distribution, (2015) 167.

651 [38] A. Bouriakova, P.S.F. Mendes, B. Katryniok, J. De Clercq, J.W. Thybaut, Co-metal induced
652 stabilization of alumina-supported copper: impact on the hydrogenolysis of glycerol to 1,2-
653 propanediol, Catalysis Communications, 146 (2020) 106134.

654 [39] A. Alhanash, E.F. Kozhevnikova, I.V. Kozhevnikov, Gas-phase dehydration of glycerol to acrolein
655 catalysed by caesium heteropoly salt, Applied Catalysis A: General, 378 (2010) 11-18.

656 [40] F. Vila, M. López Granados, R. Mariscal, Significance of isomeric reaction intermediates in the
657 hydrogenolysis of glycerol to 1,2-propanediol with Cu-based catalysts, Catalysis Science &
658 Technology, 7 (2017) 3119-3127.

659 [41] C. Montassier, J. Ménézo, L. Hoang, C. Renaud, J. Barbier, Aqueous polyol conversions on
660 ruthenium and on sulfur-modified ruthenium, Journal of Molecular Catalysis, 70 (1991) 99-110.

661 [42] H. Pines, W.O. Haag, Alumina: Catalyst and Support. I. Alumina, its Intrinsic Acidity and Catalytic
662 Activity1, Journal of the American Chemical Society, 82 (1960) 2471-2483.

663 [43] E. Vasiliadou, A. Lemonidou, Kinetic study of liquid-phase glycerol hydrogenolysis over Cu/SiO
664 2 catalyst, Chemical Engineering Journal, 231 (2013) 103-112.

665 [44] E. Vasiliadou, A. Lemonidou, Investigating the performance and deactivation behaviour of silica-
666 supported copper catalysts in glycerol hydrogenolysis, Applied Catalysis A: General, 396 (2011) 177-
667 185.

668 [45] S. Sato, M. Akiyama, R. Takahashi, T. Hara, K. Inui, M. Yokota, Vapor-phase reaction of polyols
669 over copper catalysts, Applied Catalysis A: General, 347 (2008) 186-191.

670 [46] T. Rajkhowa, G.B. Marin, J.W. Thybaut, A comprehensive kinetic model for Cu catalyzed liquid
671 phase glycerol hydrogenolysis, Applied Catalysis B: Environmental, 205 (2017) 469-480.

672 [47] A. Yin, X. Guo, W.-L. Dai, K. Fan, The Nature of Active Copper Species in Cu-HMS Catalyst for
673 Hydrogenation of Dimethyl Oxalate to Ethylene Glycol: New Insights on the Synergetic Effect between
674 Cu0 and Cu+, The Journal of Physical Chemistry C, 113 (2009) 11003-11013.

675 [48] X. Li, M. Xiang, D. Wu, Hydrogenolysis of glycerol over bimetallic CuNi catalysts supported on
676 hierarchically porous SAPO-11 zeolite, Catalysis Communications, 119 (2019) 170-175.

677 [49] K. Samson, M. Śliwa, R.P. Socha, K. Góra-Marek, D. Mucha, D. Rutkowska-Zbik, J.F. Paul, M.
678 Ruggiero-Mikołajczyk, R. Grabowski, J. Słoczyński, Influence of ZrO2 Structure and Copper
679 Electronic State on Activity of Cu/ZrO2 Catalysts in Methanol Synthesis from CO2, ACS Catalysis, 4
680 (2014) 3730-3741.

681 [50] Y. Nakagawa, M. Tamura, K. Tomishige, Perspective on catalyst development for glycerol
682 reduction to C3 chemicals with molecular hydrogen, Research on Chemical Intermediates, 44 (2018)
683 3879-3903.

684 [51] C. Liu, Z. Zhang, X. Zhai, X. Wang, J. Gui, C. Zhang, Y. Zhu, Y. Li, Synergistic effect between
685 copper and different metal oxides in the selective hydrogenolysis of glucose, New Journal of
686 Chemistry, 43 (2019) 3733-3742.

687 [52] S. Kandasamy, S.P. Samudrala, S. Bhattacharya, The route towards sustainable production of
688 ethylene glycol from a renewable resource, biodiesel waste: a review, Catalysis Science &
689 Technology, 9 (2019) 567-577.

690 [53] Y. Liu, X. Guo, G.L. Rempel, F.T.T. Ng, The Promoting Effect of Ni on Glycerol Hydrogenolysis
691 to 1,2-Propanediol with In Situ Hydrogen from Methanol Steam Reforming Using a Cu/ZnO/Al2O3
692 Catalyst, Catalysts, 9 (2019) 412.

693 [54] J. Huang, T. Ding, K. Ma, J. Cai, Z. Sun, Y. Tian, Z. Jiang, J. Zhang, L. Zheng, X. Li, Modification
694 of Cu/SiO2 Catalysts by La2O3 to Quantitatively Tune Cu+-Cu0 Dual Sites with Improved Catalytic
695 Activities and Stabilities for Dimethyl Ether Steam Reforming, ChemCatChem, 10 (2018) 3862-3871.

696 [55] X. Zheng, H. Lin, J. Zheng, X. Duan, Y. Yuan, Lanthanum oxide-modified Cu/SiO2 as a high-
697 performance catalyst for chemoselective hydrogenation of dimethyl oxalate to ethylene glycol, ACS
698 Catalysis, 3 (2013) 2738-2749.

699 [56] G. Rampelberg, B. De Schutter, W. Devulder, K. Martens, I. Radu, C. Detavernier, In situ X-ray
700 diffraction study of the controlled oxidation and reduction in the V–O system for the synthesis of VO2
701 and V2O3 thin films, Journal of Materials Chemistry C, 3 (2015) 11357-11365.

702 [57] A. Gervasini, S. Bennici, Dispersion and surface states of copper catalysts by temperature-
703 programmed-reduction of oxidized surfaces (s-TPR), Applied Catalysis A: General, 281 (2005) 199-
704 205.

705 [58] Jeol, JEM-2200FS Field Emission Electron Microscope.

706 [59] K. van der Borght, K. Toch, V. Galvita, J.W. Thybaut, G.B. Marin, Information-Driven Catalyst
707 Design Based on High-Throughput Intrinsic Kinetics, Catalysts, 5 (2015) 1948.

708 [60] J.J. Carberry, CHEMICAL REACTION ENGINEERING - Inter-Intraphase Diffusion and Chemical
709 Reaction, Industrial & Engineering Chemistry, 61 (1969) 51-53.

710 [61] P. Weisz, C. Prater, Interpretation of measurements in experimental catalysis, Advances in
711 Catalysis, Elsevier1954, pp. 143-196.

[62] R. Beerthuis, J.W. de Rijk, J.M.S. Deeley, G.J. Sunley, K.P. de Jong, P.E. de Jongh, Particle size effects in copper-catalyzed hydrogenation of ethyl acetate, Journal of Catalysis, 388 (2020) 30-37.

[63] Krijn P. de Jong, Synthesis of Solid Catalysts, 2009.

[64] K.S. Sing, D. Everett, R. Haul, L. Moscou, R. Pierotti, J. Rouquerol, T. Siemieniewska, Reporting physisorption data for gas/solid systems with special reference to the determination of surface area and porosity (Recommendations 1984), Pure appl. chem, 57 (1985) 603-619.

[65] K.S.W. Sing, R.T. Williams, Physisorption Hysteresis Loops and the Characterization of Nanoporous Materials, Adsorption Science & Technology, 22 (2004) 773-782.

[66] M. Bettman, R. Chase, K. Otto, W. Weber, Dispersion studies on the system La2O3γ-Al2O3, Journal of Catalysis, 117 (1989) 447-454.

[67] T. Mimani, Instant synthesis of nanoscale spinel aluminates, Journal of Alloys and Compounds, 315 (2001) 123-128.

[68] K.T. JACOB, C.B. ALCOCK, Thermodynamics of CuAlO2 and CuAl2O4 and Phase Equilibria in the System Cu2O-CuO-Al2O3, Journal of the American Ceramic Society, 58 (1975) 192-195.

[69] Y. Xie, D. Kocaefe, Y. Kocaefe, J. Cheng, W. Liu, The effect of novel synthetic methods and parameters control on morphology of nano-alumina particles, Nanoscale research letters, 11 (2016) 1-11.

[70] L. Samain, A. Jaworski, M. Edén, D.M. Ladd, D.-K. Seo, F. Javier Garcia-Garcia, U. Häussermann, Structural analysis of highly porous γ-Al2O3, Journal of Solid State Chemistry, 217 (2014) 1-8.

[71] P.G. Menon, J. Prasad, Exposure of metallic copper surface on Cu· Al2O3-carbon catalysts, Journal of Catalysis, 17 (1970) 238-244.

[72] A. Budiman, M. Ridwan, S.M. Kim, J.-W. Choi, C.W. Yoon, J.-M. Ha, D.J. Suh, Y.-W. Suh, Design and preparation of high-surface-area Cu/ZnO/Al2O3 catalysts using a modified co-precipitation method for the water-gas shift reaction, Applied Catalysis A: General, 462 (2013) 220-226.

[73] Y. Zhao, S. Li, Y. Wang, B. Shan, J. Zhang, S. Wang, X. Ma, Efficient tuning of surface copper species of Cu/SiO2 catalyst for hydrogenation of dimethyl oxalate to ethylene glycol, Chemical Engineering Journal, 313 (2017) 759-768.

[74] J.L. Ayastuy, A. Gurbani, M.P. González-Marcos, M.A. Gutiérrez-Ortiz, Effect of copper loading on copper-ceria catalysts performance in CO selective oxidation for fuel cell applications, International Journal of Hydrogen Energy, 35 (2010) 1232-1244.

[75] J. Lee, U.G. Hong, S. Hwang, M.H. Youn, I.K. Song, Catalytic cracking of C5 raffinate to light olefins over lanthanum-containing phosphorous-modified porous ZSM-5: Effect of lanthanum content, Fuel Processing Technology, 109 (2013) 189-195.

[76] Y. Zhu, X. Kong, B. Peng, L. Li, Z. Fang, Y. Zhu, Efficient Cu catalyst for 5-hydroxymethylfurfural hydrogenolysis by forming Cu–O–Si bonds, Catalysis Science & Technology, 10 (2020) 7323-7330.

749 [77] R.J. Chimentão, P. Hirunsit, C.S. Torres, M.B. Ordoño, A. Urakawa, J.L.G. Fierro, D. Ruiz,
750 Selective dehydration of glycerol on copper based catalysts, Catalysis Today, (2020).

751 [78] R.-P. Ye, L. Lin, Q. Li, Z. Zhou, T. Wang, C.K. Russell, H. Adidharma, Z. Xu, Y.-G. Yao, M. Fan,
752 Recent progress in improving the stability of copper-based catalysts for hydrogenation of carbon–
753 oxygen bonds, Catalysis Science & Technology, 8 (2018) 3428-3449.

754 [79] H. Yue, X. Ma, J. Gong, An Alternative Synthetic Approach for Efficient Catalytic Conversion of
755 Syngas to Ethanol, Accounts of Chemical Research, 47 (2014) 1483-1492.

756 [80] M. Behrens, S. Zander, P. Kurr, N. Jacobsen, J.r. Senker, G. Koch, T. Ressler, R.W. Fischer, R.
757 Schlögl, Performance improvement of nanocatalysts by promoter-induced defects in the support
758 material: methanol synthesis over Cu/ZnO: Al, Journal of the American Chemical Society, 135 (2013)
759 6061-6068.

760 [81] Z. Huang, F. Cui, H. Kang, J. Chen, X. Zhang, C. Xia, Highly dispersed silica-supported copper
761 nanoparticles prepared by precipitation– gel method: a simple but efficient and stable catalyst for
762 glycerol hydrogenolysis, Chemistry of Materials, 20 (2008) 5090-5099.

763 [82] M.L. Dieuzeide, R. de Urtiaga, M. Jobbagy, N. Amadeo, Vapor phase hydrogenolysis of glycerol
764 to 1,2-propanediol at atmospheric pressure over copper catalysts supported on mesoporous alumina,
765 Catalysis Today, 296 (2017) 19-25.

766 [83] X. Li, Q. Zhang, H. Xie, X. Gao, Y. Wu, G. Yang, P. Wang, S. Tian, Y. Tan, Facile Preparation of
767 Cu-Al Oxide Catalysts and Their Application in the Direct Synthesis of Ethanol from Syngas,
768 ChemistrySelect, 2 (2017) 10365-10370.

769 [84] M.G. Mason, Electronic structure of supported small metal clusters, Physical Review B, 27 (1983)
770 748-762.

771 [85] V. Di Castro, C. Furlani, M. Gargano, N. Ravasio, M. Rossi, XPS study of copper dispersion in
772 CuO/Al2O3 catalysts, Journal of Electron Spectroscopy and Related Phenomena, 52 (1990) 415-
773 422.

774 [86] M.C. Biesinger, Advanced analysis of copper X-ray photoelectron spectra, Surface and Interface
775 Analysis, 49 (2017) 1325-1334.

776 [87] J. Gong, H. Yue, Y. Zhao, S. Zhao, L. Zhao, J. Lv, S. Wang, X. Ma, Synthesis of ethanol via
777 syngas on Cu/SiO2 catalysts with balanced Cu0–Cu+ sites, Journal of the American Chemical
778 Society, 134 (2012) 13922-13925.

779